PHYSICAL REVIEW E **83**, 045401(R) (2011)

Transverse plasma-wave localization in multiple dimensions

J. E. Fahlen,[1,*] B. J. Winjum,[2] T. Grismayer,[2] and W. B. Mori[1,2]
[1]*Department of Electrical Engineering, University of California, Los Angeles, California 90095, USA*
[2]*Department of Physics and Astronomy, University of California, Los Angeles, California 90095, USA*
(Received 7 May 2010; published 15 April 2011)

Plasma-wave behavior in multiple dimensions is studied using two- and three-dimensional particle-in-cell simulations. We find that large-amplitude waves with $k\lambda_D \gtrsim 0.2$, where k is the wave number of the wave and λ_D is the Debye length, localize in the transverse direction around their axis due to nonlinear, local damping caused by transiting particles. The center of the wave behaves like a plane wave in which trapped particles maintain a quasisteady state at approximately constant amplitude, while the transverse edges damp away.

DOI: 10.1103/PhysRevE.83.045401 PACS number(s): 52.35.Fp, 52.35.Mw, 52.38.Bv, 52.65.Rr

The linear and nonlinear evolution of infinitely long plasma waves has been studied extensively. Despite the fact that actual plasma waves have finite longitudinal and transverse extent, the study of plasma waves in multiple dimensions has received little attention. Recently, however, the transverse localization of such waves was cited as a possible saturation mechanism [1] of stimulated Raman scattering (SRS) [2]. Reference [1] attributed this localization to plasma-wave self-focusing caused by the wavefront bowing that results from the nonlinear trapped-particle frequency shift [3,4].

Beyond SRS, the evolution of multidimensional, nonlinear plasma waves of finite spatial extent is fundamentally important to a wide range of plasma physics research. In this Rapid Communication, we provide a fully kinetic analysis of multidimensional plasma waves and show the mechanism responsible for their transverse localization. We find that the localization caused by wavefront bowing is dominated by that due to multidimensional wave-particle interactions: particles that originate outside the wave locally damp its edges as they traverse it. We demonstrate this in part by showing how energy flows in such waves. We provide quantitative agreement between the simulations and fluid theory ($k\lambda_D \ll 1$) and then consider in detail how local damping dominates self-focusing at shorter wavelengths ($k\lambda_D \gtrsim 0.2$).

Previous work on nonlinear plasma waves is extensive and has a long history; see, for example, [5]. In one dimension (1D), nonlinear frequency shifts, due to either harmonic generation [6] or particle trapping [7–9], and self-generated density modifications due to the ponderomotive force, have been studied. In multiple dimensions, the effects of density modulations have been studied using the Zakharov equations [10,11]. This model requires $k\lambda_D \ll 1$ and assumes that the wave's transverse ponderomotive force digs a density depression that concentrates its energy. As the waves collapse to higher $k\lambda_D$, kinetic effects like Landau damping and transit-time damping [12] are modeled with phenomenological fluid damping terms [13] or quasilinear approximations [14]. For the waves considered here, $k\lambda_D \gtrsim 0.2$, and nonlinear kinetic effects dominate the wave's behavior before Langmuir collapse begins. In attempting to extend kinetic effects to multiple dimensions, some authors have inserted the 1D expression for the frequency shift [7] into a nonlinear Schrödinger equation (NLS) model. Such models can lead to so-called trapped-particle modulational instabilities (TPMI) [3,4] in 1D, and wavefront bowing and self-focusing in two and three dimensions (2D and 3D) [1]. Importantly, these models rely on a frequency shift that is a function of the local and instantaneous wave amplitude. This is not always valid for finite-size waves, and one must then rely on fully kinetic simulation models.

In this Rapid Communication, we use 2D and 3D particle-in-cell (PIC) simulations to study kinetic plasma waves with finite transverse extent and $k\lambda_D \gtrsim 0.2$. We use the electrostatic PIC code BEPS with 256×4096 cells, $\Delta_x = \Delta_y = \lambda_D$, $\Delta_t = 0.2\omega_p^{-1}$, and 2000 particles per cell. An externally imposed ponderomotive driver excites a traveling wave with a Gaussian or super-Gaussian profile defined by $E_x = E_0 e^{-y^n/2W_0^n} \sin(kx - \omega t)$, with $n = 2$ and 4, respectively, k is the wave number, ω is the frequency, and we define the phase velocity $v_\phi = \omega/k$ for use below. For each simulation, we choose (Ω,k) to satisfy $\epsilon(\Omega,k) = 0$, where ϵ is the kinetic dielectric function that includes a finite-size-particle shape factor and $\omega = \mathrm{Re}[\Omega]$. We also specify an amplitude and a transverse profile. The initial width W_0 is chosen to approximate the ponderomotive force of a typical $f/8$ beam at the National Ignition Facility (NIF) undergoing SRS. The driver is on for about two wave periods before it shuts off. The amplitudes of some waves discussed below fall below the thermal fluctuations of the field. To observe them, we subtract the field obtained from an identical simulation in which the driver is turned off [15]. We have repeated a few simulations with Darwin and electromagnetic codes based on the UCLA Parallel Particle-in-Cell (UPIC) Framework [16] with $v_{\mathrm{th}}/c = 0.1$ and observed quantitatively similar results. The ions are fixed in the following, but simulations with mobile ions also yield quantitatively similar results.

To illustrate transverse localization, in Fig. 1 we plot the longitudinal electric field E_x at four times for a wave with $k\lambda_D = 0.3$, a super-Gaussian transverse profile ($n = 4$) with $W_0 = 200\lambda_D$, and peak initial amplitude $eE/m\omega_p v_{\mathrm{th}} = 0.079$, or equivalently $\gamma_L/\omega_B = 0.095$, where $\omega_B = \sqrt{eEk/m}$ is the trapped-particle bounce frequency and γ_L is the Landau damping rate. The wave maintains a fairly constant amplitude along its center as the boundaries (edges) gradually converge (localize) toward the central axis. Nonlinear plane-wave (1D)

*jfahlen@ucla.edu

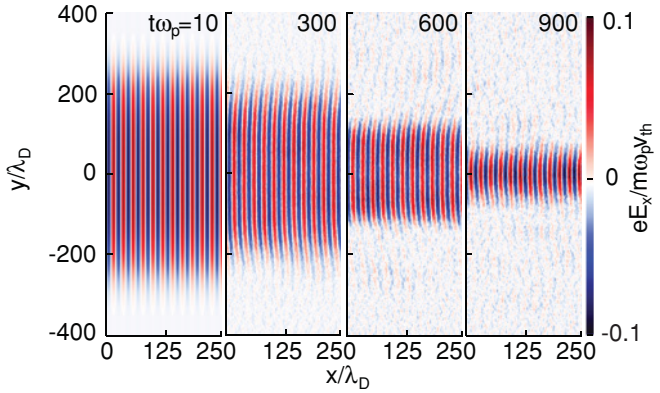

FIG. 1. (Color) Time sequence of $E_x(x,y)$ for a wave with $k\lambda_D = 0.3$, $W_0 = 200\lambda_D$, peak amplitude $eE/m\omega_p v_{\rm th} \approx 0.079$, and super-Gaussian profile ($n = 4$).

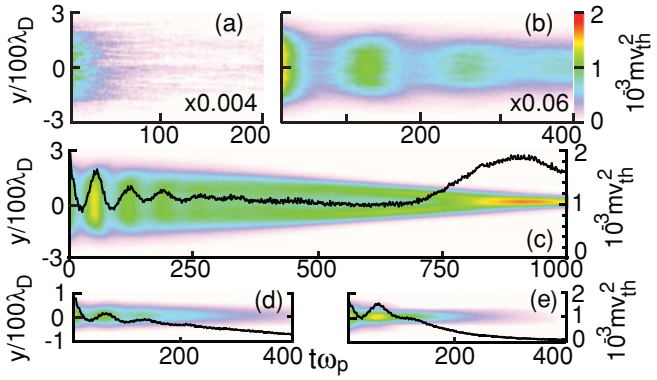

FIG. 2. (Color) $\langle U(x,y,t)\rangle_x$ for runs with $k\lambda_D = 0.3$ and $eE/m\omega_p v_{\rm th} = 0.004$, 0.02, and 0.079, or $\gamma_L/\omega_B = 0.42$, 0.19, and 0.095 in (a), (b), and (c), respectively. Case (c) corresponds to the case in Fig. 1. Cases (d) and (e) correspond to $t\omega_p = 750$ in (c), but with a Gaussian profile and $W_0 = 40\lambda_D$; cases (d) and (e) have $n = 2$, and (e) has $b = 2$.

theory [7,17] suggests that waves having $\gamma_L/\omega_B \ll 1$ reach a nonlinear steady state after the resonant particles that are trapped in the wave's potential wells have executed several trapped-particle oscillations. Thus, the wave in Fig. 1 reaches a steady state quickly. 1D kinetic theory also predicts that particle trapping induces a negative, amplitude-dependent frequency shift [7], so the center of a finite-width wave accumulates a relative phase shift with respect to the edges that causes the wavefronts to bend inward [1,3,4], as seen in Fig. 1.

In the following, we first show that the center of finite-width waves reaches this steady state once their initial amplitude is increased beyond linear levels ($\gamma_L/\omega_B \approx 1$) to ranges where $\gamma_L/\omega_B \ll 1$. We then describe how a nonlinear local damping mechanism leads to erosion of the wave's edges with or without wavefront bending. For clarity, we use the case shown in Fig. 1 for the majority of the figures in this Rapid Communication. However, although not shown, similar behavior occurs for a range of parameters satisfying $k\lambda_D \gtrsim 0.2$, $\gamma_L/\omega_B \ll 1$, and a variety of transverse profiles and widths.

At low amplitudes, when $\gamma_L/\omega_B \approx 1$, finite-width waves Landau damp with no notable differences from plane waves. To demonstrate this, in Fig. 2(a) we show $\langle U(x,y,t)\rangle_x$ for a wave with $\gamma_L/\omega_B \approx 0.42$, where $U = \frac{1}{2}\mathbf{E}\cdot\mathbf{E}$ and the brackets indicate an average over a wavelength. We have normalized the energy to $mv_{\rm th}^2$ and E to $e/m\omega_p v_{\rm th}$. As shown in Fig. 2(b) for $\gamma_L/\omega_B \approx 0.19$, at slightly larger amplitudes particles trap, causing a significant fraction of the wave's energy to be absorbed before bouncing and returning some of it. For early times, $t \lesssim \tau_B/4$, the wave Landau damps with $\gamma_{\rm sim}/\gamma_L \approx 1.1$, which is within the measurement error, where $\gamma_{\rm sim}$ is the measured damping rate in the simulation and $\tau_B = 2\pi/\omega_B$. From Fig. 2(b), we estimate $\tau_B\omega_p \approx 100$, which gives a thermal particle sufficient time to cross much of the wave during a bounce time, i.e., $v_{\rm th}\tau_B \gtrsim W_0$. Thus, many of the resonant particles that absorb wave energy during the first $\tau_B/4$ either leave the wave or do not become trapped because of the decreased depth of their potential well. Accordingly, the amplitude at each successive bounce time decreases until the wave disappears.

For the two low-amplitude cases described above, both Landau damping and the modulation of the wave amplitude are due primarily to particles that were initialized within the wave. At each transverse position, the wave behaves as if it were an isolated, 1D wave. However, when $\gamma_L/\omega_B \ll 1$, after the first few bounce times, multidimensional effects become important. This is shown in Fig. 2(c) for the same wave shown in Fig. 1. The center of this wave still behaves like a plane wave since thermal particles bounce many times while still inside the wave ($v_{\rm th}\tau_B \approx 40\lambda_D \approx W_0/5$). Accordingly, the wave exists for a relatively long time, allowing novel multidimensional effects to appear. The dominant new effect, as can also be seen in Fig. 1, is the gradual localization of the wave in the transverse direction while the central amplitude [the black line in Fig. 2(c)] remains nearly constant until $t\omega_p \approx 700$. That is, the central section shows 1D-like behavior, while the sides locally damp. For $t\omega_p \gtrsim 700$ in Fig. 2(c), the wave continues to localize, but an intensity enhancement also occurs. Although it is qualitatively similar to the effects of self-focusing, a local, instantaneous self-focusing model is inadequate to describe the behavior. To see this, we show two waves in Figs. 2(d) and 2(e) with $W_0 = 40\lambda_D$ and Gaussian profiles that attempt to reproduce the behavior of the wave in (c) at $t\omega_p \approx 700$. In (e), the wave was initialized with inwardly bent wavefronts defined by $\phi = \phi_0 e^{-y^2/2W_0^2}\sin(kx - \omega t + be^{-y^2/4W_0^2})$ and $b = 2$ that mimic the bending seen in (c) at late times. In both cases, the wave quickly damps away in contrast to the late-time behavior of the wave shown in (c), whose amplitude abruptly increases before falling again. These two cases illustrate that the wave's behavior is not solely dependent on the instantaneous, local amplitude.

To understand the behavior of a nonlinear wave, one needs to understand in detail how energy flows and dissipates in multiple dimensions. The natural starting point is to examine the conservation of both field and kinetic energy. We note that the Poynting vector $\mathbf{S} = \frac{1}{4\pi}\mathbf{E}\times c\mathbf{B}$, written here in cgs units, does not vanish in the electrostatic limit because, although $\mathbf{B} \to \mathbf{0}$, the speed of light $c \to \infty$ such that $c\mathbf{B}$ is not necessarily 0. As shown by Decyk [18], an expression for the electrostatic Poynting vector is $\mathbf{P} = \phi(\mathbf{j} + \frac{1}{4\pi}\partial_t\mathbf{E})$. Thus, the equation expressing conservation of field energy

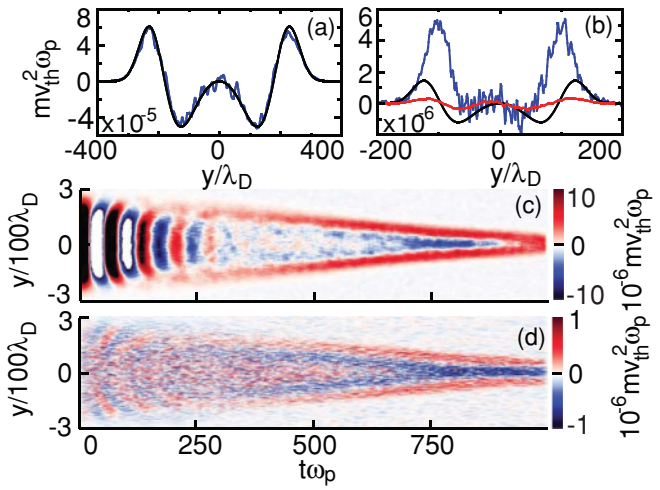

FIG. 3. (Color) (a) $\langle \mathbf{j}\cdot\mathbf{E}\rangle_x$ in blue, $\langle \mathbf{j_1}\cdot\mathbf{E_1}\rangle_x$ in black at $t\omega_p = 40$; (b) $\langle \mathbf{j}\cdot\mathbf{E}\rangle_x$ in blue, $\langle \mathbf{j_1}\cdot\mathbf{E_1}\rangle_x$ in black, and $\langle \nabla\cdot\mathbf{P}\rangle_x$ in red at $t\omega_p = 600$; (c) $\langle \mathbf{j}\cdot\mathbf{E}\rangle_x$; and (d) $\langle \nabla\cdot\mathbf{P}\rangle_x$. All cases have the same parameters as Fig. 1 except (a), which has $k\lambda_D = 0.1$.

is $\partial_t U + \nabla\cdot\mathbf{P} = -\mathbf{j}\cdot\mathbf{E}$, where we have used electrostatic units defined as $e\mathbf{E}/m\omega_p v_{\rm th}$, $t\omega_p$, $\mathbf{x}/\lambda_D$, and $\mathbf{P}/mn_0v_{\rm th}^3$. It is possible to rewrite $\mathbf{j}\cdot\mathbf{E}$ in a useful form in the fluid limit. Inserting Euler's equation, given by $\partial_t\mathbf{v} + \mathbf{v}\cdot\nabla\mathbf{v} = -\mathbf{E} - \frac{3}{2}\nabla n^2$, into $\mathbf{j}\cdot\mathbf{E}$, we find the expression for conservation of kinetic energy, given by $\mathbf{j}\cdot\mathbf{E} = \partial_t U_k + \nabla\cdot\mathbf{P_k}$, where $U_k = \frac{1}{2}(nv^2 + n^3)$, $\mathbf{P_k} = \frac{1}{2}(nv^2\mathbf{v} + 3n^3\mathbf{v})$, $v = |\mathbf{v}|$, $\mathbf{j} = -n\mathbf{v}$, and we have assumed the adiabatic equation of state for the electrons. Substituting this result for $\mathbf{j}\cdot\mathbf{E}$ back into the conservation of energy equation gives $\partial_t(U + U_k) + \nabla\cdot(\mathbf{P} + \mathbf{P_k}) = 0$. An energy transport velocity is defined by $\mathbf{v_E} = \langle \mathbf{P} + \mathbf{P_k}\rangle_t / \langle U + U_k\rangle_t$. In a plane wave, the magnetic field rigorously vanishes so that $\mathbf{P} = \mathbf{0}$. Under this condition, it can be shown for fluid quantities of a linear wave that $\mathbf{v_E} = 3\mathbf{k}/\omega = \mathbf{v_g}$, where $\mathbf{v_g}$ is the linear group velocity.

For curved wavefronts $\mathbf{P} \neq \mathbf{0}$, and the direction of $\mathbf{v_g}$ can vary with the transverse position. However, as verified in the simulations (see below), $|\mathbf{P}| \ll |\mathbf{P_k}|$. In addition, there is roughly equipartition between the field and kinetic energy, $U \approx U_k$. Therefore, $\mathbf{j}\cdot\mathbf{E} \approx \nabla\cdot\mathbf{P_k}/2$ so that we can understand the total wave energy flux by examining only $\mathbf{j}\cdot\mathbf{E}$.

For example, in Fig. 3(a) we plot $\langle \mathbf{j}\cdot\mathbf{E}\rangle_x$ from a simulation for which the fluid approximation is reasonable, $k\lambda_D = 0.1$, $b = 5$, $W = 200\lambda_D$, and $eE/m\omega_p v_{\rm th} = 0.61$. This corresponds to a wave with the wavefronts bent inwards. The blue line in Fig. 3(a) shows $\langle \mathbf{j}\cdot\mathbf{E}(t\omega_p = 40)\rangle_x$ from the simulation, while the black curve shows $\langle \mathbf{j_1}\cdot\mathbf{E_1}\rangle_x$ calculated using the linear fluid quantities for the initial wave profile. Here, the subscript "1" represents the linear quantity. Since there is no damping for small $k\lambda_D$, $\mathbf{j}\cdot\mathbf{E}$ is proportional to the divergence of the total energy flux. There is excellent agreement between the linear fluid theory and the simulation, lending confidence that the fluid theory calculation gives an accurate estimate of the energy flow caused by wavefront bending. The fact that wave energy is flowing coherently can be seen by noting that wherever $\langle \mathbf{j}\cdot\mathbf{E}\rangle_x$ is positive, there is an adjacent region in which it is negative, or $\int\langle \mathbf{j}\cdot\mathbf{E}\rangle_x dy = 0$. That is, energy that left one region entered another nearby region and was not dissipated.

We next examine $\mathbf{j}\cdot\mathbf{E}$ for $k\lambda_D = 0.3$, where collisionless dissipation from wave-particle interactions is possible. In Fig. 3(b), we show $\langle \mathbf{j}\cdot\mathbf{E}\rangle_x$ calculated from the simulation in Fig. 1 in blue at $t\omega_p = 600$. The black curve is $\langle \mathbf{j_1}\cdot\mathbf{E_1}\rangle_x$ calculated from the linear fluid equations with $b = 4$ to approximate the bending seen in the simulation. In this case, there are dramatic differences between the simulation and the fluid prediction, and $\int\langle \mathbf{j}\cdot\mathbf{E}\rangle_x dy \neq 0$, indicating dissipation. From the plot of $\langle \mathbf{j}\cdot\mathbf{E}\rangle_x$, it is clear this dissipation occurs locally at the edge of the wave. We also plot the temporal evolution of $\langle \mathbf{j}\cdot\mathbf{E}\rangle_x$ versus y in Fig. 3(c) to show that the wave gradually localized due to the continued dissipation of energy at the wave's edge. In Fig. 3(d), we plot $\langle \nabla\cdot\mathbf{P}\rangle_x$ from the simulation and its lineout in Fig. 3(b). These plots show that $\int\langle \nabla\cdot\mathbf{P}\rangle_x dy \approx 0$, consistent with $\nabla\cdot\mathbf{P}$ being related to the energy flux, rather than the loss of energy, and that $\langle \nabla\cdot\mathbf{P}\rangle_x \ll \langle \nabla\cdot\mathbf{P_k}\rangle_x$, which implies that $\langle \nabla\cdot\mathbf{P}\rangle_x \ll \langle \mathbf{j}\cdot\mathbf{E}\rangle_x$.

From the above, it appears that localization is primarily due to local dissipation rather than self-focusing. Another demonstration that this is true is to compare the measured $U_{\rm axis}(t) = \langle U(x, y = 0, z = 0, t)\rangle_x$ with what we would expect were the field energy conserved during localization as it is in self-focusing. In this case, we would find in 2D that $U_{\rm axis}(t) = U_0 W_0/W(t)$ and in 3D that $U_{\rm axis}(t) = U_0[W_0/W(t)]^2$, where $U_0 = U_{\rm axis}(t = 0)$. Thus, the concentration of energy is exaggerated in 3D. We measure $W(t)$ in the simulations by finding the y position such that $U(y,t) = U_{\rm axis}(t)e^{-1}$. The top of Fig. 4 shows isosurfaces of $\langle U(x,y,z,t)\rangle_x$ of a 3D simulation with a Gaussian profile, $W_0 = 200\lambda_D$, $k\lambda_D = 0.3$, and peak amplitude $eE/m\omega_p v_{\rm th} \approx 0.1$. The bottom plot shows, on the left axis, $U_{\rm axis}(t)$ for the 3D wave labeled "U 3D" and for the 2D wave in Fig. 1 ("U 2D SG"). The dashed lines are the on-axis amplitude assuming self-focusing was occurring, or $U_{\rm axis}(t)$ calculated using the measured $W(t)$ for each case ("W 3D" and "W 2D SG"). We also show $W(t)$ for an identical 2D run with a Gaussian profile ("U 2D G"). We note that all three cases localize at approximately the same rate despite having different

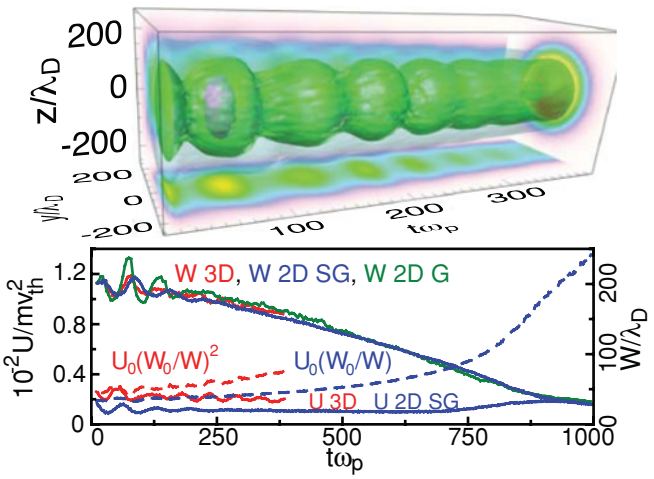

FIG. 4. (Color) The upper plot is $\langle U(x,y,z,t)\rangle_x$, with arbitrary color scale units. The lower plot shows $\langle U(x, y = 0, z = 0, t)\rangle_x$ on the left axis and W on the right. See the text for label definitions.

profiles and dimensionality. As seen in the figure, the measured energies are much smaller than would be observed were self-focusing responsible for localization. The 3D simulation used a grid $256 \times 1024 \times 1024$ with 2.58×10^{10} particles with periodic boundary conditions that limit the duration of the simulation.

Previously we showed where the local damping occurs by plotting $\langle \mathbf{j} \cdot \mathbf{E} \rangle_x$ in Fig. 3(c), but we have not shown which particles cause it. We again plot $\langle \mathbf{j} \cdot \mathbf{E} \rangle_x$ versus y in Fig. 5(a) for the same case, except now only the contribution from those particles with initial conditions $y_i < -400\lambda_D$ and $v_{yi} > 0$ is included. This figure shows that transiting particles that start below the wave and move upward through it on average absorb energy as they enter and return a fraction of what was absorbed as they leave. Particles that originate above the wave moving downward behave the same, such that there is a net energy loss at the wave's edges. By studying these particles, we can identify which absorb the wave energy. As in 1D theory, v_x only changes for particles within the 1D trapping width $v_T(y = 0) \approx v_{\rm th}$ around $v_\phi = 3.8v_{\rm th}$. This is shown in Fig. 5(b), which plots v_{xf} versus v_{xi}, where the "final" velocity is measured when the particle satisfies $y > 400\lambda_D$, and the cross corresponds to the lines $v_{xf} = v_{xi}$ and $v_{xf} = 2v_\phi - v_{xi}$ within the trapping width. Figure 5(c) shows v_y changes little for the transiting particles, since $|E_y| \propto y|E_x|/kW_0^2$. Figure 5(d), showing the distribution function versus v_{xf} for three different v_{yi}, indicates that the trapping occurs for all v_{yi}. Thus, we confirm that the bulk of the particles execute many bounce times as they cross the wave since $v_{\rm th}\tau_B \approx W_0/5$. Although not shown, this is also clearly seen in individual particle tracks. It is these particles that sustain the center of the wave. Figure 5(d) also indicates that, although there are initially more particles with $v_{yi} = v_{\rm th}$ than $2v_{\rm th}$, slightly fewer of those particles have reached $y = 400\lambda_D$ by the end of the simulation. This shows that the damping depends on the particle flux, rather than simply the local distribution, and serves to illustrate the complexity of the local damping. We

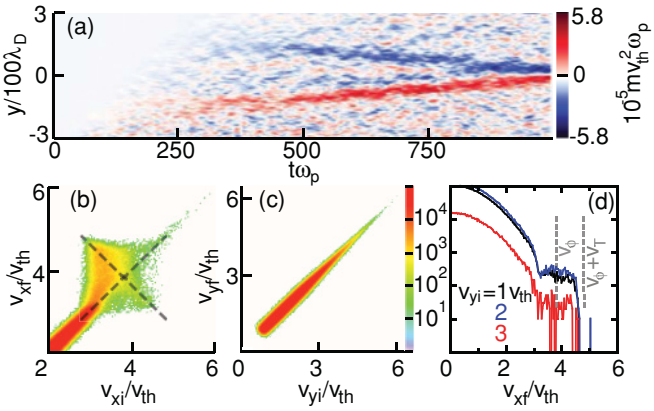

FIG. 5. (Color) Results for particles transiting upward: (a) $\langle \mathbf{j} \cdot \mathbf{E} \rangle_x$, (b) v_{xf} vs v_{xi}, (c) v_{yf} vs v_{yi}, and (d) $f(v_{xf})$ for v_{yi} =1, 2, and $3v_{th}$, each for the same wave shown in Fig. 1. The values for the color scale are also the values for the y axis of (d).

can further examine the distribution in Fig. 5(b) by considering energy conservation for the transiting particles in the wave frame. In a fixed amplitude wave, if $v_{yi} = v_{yf}$, then $v_{xf} = v_{xi}$ or $2v_\phi - v_{xi}$. However, in the simulation we measure the average magnitude energy change to be $0.3mv_{\rm th}^2$ per particle. This deviation from energy conservation (due to the changing wave amplitude during localization) combined with the small spread of v_{yf} at a given v_{yi} (with a full width at half-maximum of $\approx 0.22v_{\rm th}$) shown in Fig. 5(c) generates the spread of v_{xf} around the cross pattern that would be expected if energy were conserved and $v_{yf} = v_{yi}$.

We thank Dr. V. K. Decyk for providing the simulation code BEPS and for his insight, and Professor G. J. Morales for stimulating discussions. This work was supported by DE-FG52-09NA29552 and NSF-Phy-0904039. Simulations were performed on the Dawson and Hoffman2 clusters at UCLA.

[1] L. Yin, B. J. Albright, K. J. Bowers, W. Daughton, and H. A. Rose, Phys. Plasmas **15**, 013109 (2008); Phys. Rev. Lett. **99**, 265004 (2007).
[2] D. W. Forslund, J. M. Kindel, and E. L. Lindman, Phys. Fluids **18**, 1002 (1975), and references therein.
[3] R. L. Dewar, W. L. Kruer, and W. M. Manheimer, Phys. Rev. Lett. **28**, 215 (1972).
[4] H. A. Rose, Phys. Plasmas **12**, 012318 (2005).
[5] J. M. Dawson, Phys. Rev. **113**, 382 (1959).
[6] B. J. Winjum, J. Fahlen, and W. B. Mori, Phys. Plasmas **14**, 102104 (2007).
[7] G. J. Morales and T. M. O'Neil, Phys. Rev. Lett. **28**, 417 (1972).
[8] D. Bénisti and L. Gremillet, Phys. Plasmas **14**, 0423304 (2007); D. Bénisti, D. J. Strozzi, and L. Gremillet, *ibid.* **15**, 030701 (2008).
[9] R. R. Lindberg, A. E. Charman, and J. S. Wurtele, Phys. Plasmas **14**, 122103 (2007).
[10] D. L. Newman, P. A. Robinson, and M. V. Goldman, Phys. Rev. Lett. **62**, 2132 (1989).
[11] P. A. Robinson, D. L. Newman, and M. V. Goldman, Phys. Rev. Lett. **61**, 702 (1988).
[12] G. J. Morales and Y. C. Lee, Phys. Rev. Lett. **33**, 1534 (1974).
[13] D. Russell, D. F. DuBois, and H. A. Rose, Phys. Rev. Lett. **60**, 581 (1988).
[14] D. F. DuBois, D. Russell, and H. A. Rose, Phys. Plasmas **2**, 76 (1995), and references therein.
[15] V. K. Decyk, Invited Paper at International Conference on Plasma Physics, Kiev, USSR, 1987.
[16] V. K. Decyk, Comput. Phys. Commun. **177**, 95 (2007).
[17] J. Canosa and J. Gazdag, Phys. Fluids **17**, 2030 (1974).
[18] V. K Decyk, Phys. Fluids **25**, 1205 (1982).